Babylonian Journal of Mathematics
Vol. **2024**, **pp.** 19–33
DOI:https://doi.org/10.58496/BJM/2024/003; ISSN:3006-113X
https://mesopotamian.press/journals/index.php/mathematics

Research Article

UTLIZATION OF GENERALIZED HEAT FLUX MODEL ON THERMAL TRANSPORT OF POWELL-EYRING MODEL VIA OHAM WITH HEAT GENEARTION ASPECTS*

Esha Rafique[1,*], Nida Ilyas[1], Muhammad Sohail[1],

[1] *Institute of Mathematics, Khwaja Fareed University of Engineering & Information Technology, Rahim Yar Khan 64200, Pakistan.*

ARTICLEINFO

Article History

Received 27 Nov 2023
Accepted 21 Jan 2024
Published 20 Feb 2024

Keywords

Three-dimensional rotating flow

Non-Fourier heat flux
Magnetohydrodynamic
Thermal radiation

Heat generation/absorption
Eyring-Powell nanofluid
Non-Fick's mass flux

ABSTRACT

The focus of this work is on the flow of a spinning Powell-Eyring nanofluid in the boundary layer in three dimensions using magnetohydrodynamics (MHD). The research simulates mass transfer processes and heat transfer processes using non-Fick's mass flux theory and non-Fourier heat flux theory, respectively. Heat transport phenomena are analyzed by the integration of non-linear heat generation/absorption and thermal radiation properties. The boundary layer method is employed to solve a system of nonlinear partial differential equations (PDE) in the mathematical formulation. These equations are converted into nonlinear ordinary differential equations (ODES), and then the optimal OHAM with convergence control parameters is used to solve them. The impact of various physical movement circumstances on concentration and temperature profiles is visually represented through the generation of diagrams. This study provides important new understandings for both applied and scholarly research on complex heat transfer and fluid dynamics mechanisms in the context of three-dimensional MHD boundary layer flows of rotating Powell-Eyring nanofluids.

1. INTRODUCTION

The dispersion of tiny particles (with a minimum size smaller than 100 nm) in a starting material with more effective heating, rheological, and water absorption characteristics is referred to as a nanofluid, as defined by Chakraborty and Panigrahi [1]. This fluid enhances the effectiveness of multiple programmes, including improved oil reclamation, drug administration, heat transmission, and lubrication. Ibrahim and Shankar [2] examined the consequences of a magnetized field, a slipping barrier situation, and heating radiation upon the boundary barrier movement and thermal exchange over a perforated stretched surface caused by a tiny fluid. The dual-phase Casson nanofluid flowing across a stretched film over an impermeable substrate was studied by Sabir et al. [3] to investigate the impact of gyrotactic bacteria and chemical processes. Sheremet et al. [4] explored the inherent convective of nano-fluid computationally in a three-dimensional container made of a hollow substance. Their results showed that Sherwood's and Nusselt values increased in tandem with Rayleigh's. Niihara [5] claims that the use of nanomaterials enhances thermal characteristics. In the study by Asirvatham et al. [6], faster communication of energy carried on by improved thermophysical properties and disordered transport of particles is primarily responsible for the increase in thermal transfer generated by tiny fluids. Mittal et al. [7] computationally examined the combined convection of a combined nano-fluid inside a perforated container containing a movable core. Their findings indicate that the addition of nanomaterials rises the convective warmth transmission ratio of the fundamental liquid.

A computational framework identified as the Eyring-Powell fluid is applied to explain the passage of non-Newtonian liquids, including blood circulation, suspensions, polymeric strategies, and medication administration. The 2-dimensional MHD circulation of the Eyring-Powell liquid paradigm approaching an expanded sheet was studied by Akbar et al. [8]. Mustafa [9] investigated the texture within a large cylindrical tube using the not-Newtonian physiological simulation of the Eyring–Powell liquid. The behavior of an Eyring-Powell tiny fluids isolated containing microbes over a surface, wedges, and stationary spot are investigated by Sumithra et al. [10]. It is seen that on the velocity histories, the Eyring-Powell liquid material coefficients λ_1 and λ_2 show opposite behaviour. In the study of fluid behavior, Umar et al. [11]

---

*Corresponding author. Email: esharafique77@gmail.com studied a 3-dimensional Eyring-Powell liquid having activating energy across a stretched sheet with slide. The basic equations for Eyring-Powell are modelled in circular coordinates with a presumption of a significant wavelength with a small Reynolds quantity estimation, as investigated by Nadeem et al. [12]. The movement and thermal transmission of Eyring Powell liquid across a constantly changing substrate in the context of an open stream velocities were studied by Hayat et al. [13]. The unstable boundary layer circulation of a spinning Eyring-Powell substance over a revolving funnel caused by the coupled impacts of transferring mass and warmth was explored by Nadeem and Saleem [14]. Seyedi et al. [15] examined radiation, chemical reactions, and heat production and absorption impacts when examining the unstable mass and heat transfer of magnetohydrodynamics Eyring Powell compressing stream in a vessel. Aneja [16] uses not-Fick's mass transport concept and not-Fourier's thermal flux idea for energy transportation and mass transport operations. In order to address several shortcomings of the well-known Fick's Law and Fourier's Law, this hypothesis is now being researched. Thermal and concentration relaxation periods are the amended variables in regular regulations, correspondingly.

The warmth equations are formulated using the non-Fourier heat flow approach, as stated by Shaik et al. [17]. This kind of undulating hollow research is appropriate for use in subterranean wire structures, building stones, biochemical device mass and heat transfer, and microelectronic gadget cooling circuits. Ibrahim [18] studied the 3-D boundary layer circulation of a turning Powell-Eyring tiny fluids. Non-Fourier thermal flux and non-Fick's mass hypothesis exchange concept are used in modelling heat transfer procedures. Mabood et al. [19] assessed the movement of tiny fluids across an unstable strengthened extending paper. They integrate non-Fourier's and non-Fick's mass warmth transition for mass and heat movement assessment. Ibrahim et al. [20] reviewed the travel of micro-polar tiny fluids through a spinning disc using non-Fick's and non-Fourier's warmth masses fluctuation theories. Nasir et al. [21] discovered the Cattaneo–Christov (not-Fickian and not-Fourier) dual dispersion theory in the preparations for heat and classes management, to regulate additional specifically hotness and concentration deliveries with thermal and solute reduction periods. Malik et al. [22] observed the features of Cattaneo-Christov dual dispersal concept to the Sisko liquid movement across a smooth elongating surface. Loganathan et al. [23] explicated the impacts of Magnetohydrodynamic Maxwell liquid with the existence of radiant energy over a fiery shallow with Cattaneo-christov dual dispersion.

The research of electrically conductive liquids in the direction of a field of magnetism is acknowledged as magneto-hydrodynamics. The majority of expected investigations on electrically-conductive streams show that their thermal transferring properties are drastically altered when a magnetic field is introduced. Thermal exchange mechanisms, nuclear reactors, and power plants are a few real-world examples of devices that use fluid movement in a magnetism field [24-25]. The real-world implications of magneto-hydrodynamics (MHD) in nuclear power plants, MHD engines, blood stream evaluation, accelerations, and MHD flows meters make the investigation of MHD movement in pipes crucial. It is difficult to determine the analytically findings for paired systems for the complicated region in the majority of real-world situations. Hartmann zones can appear, as suggested by Prasanna Jeyanthi and Ganesh [26], when a stream passes through an area with an abnormally high magnetic field, such as the bounding area of an atomically fusing reactors. The constant smooth MHD flows across the annulus cross-sectional was studied by Sohet [27]. Unstable MHD movement of a dirty liquid among adjacent permeable surfaces within angular velocity was examined by Delhi Babu et al. [28]. The preliminary research on MHD motion via an enclosed toroidal squared curvy medium under turbulence and smooth circumstances was examined by Moresco and Alboussière [29]. In the existence of a magnetized field, Vimala and Manimegalai [30] studied the combined convective uniform movement of an inflexible tiny fluids.

The ability to track radiant heat is important for many applications. Li and Fan [31] considered the intriguing possibility of warmth implements because the warmth qualities of nanophotonic structures, in which preferable structural elements are at a subwavelength scales or dimensions, may be quite distinct from the ones of standard warmth manufacturers. Safaei et al. [32] studied the relationship amongst thermal external radiation and Nanoscale liquid free convective in a 2-D long cavity utilizing the lattice Boltzmann approach. Al-Khaled et al. [33] examined a tangential hyperbola tiny liquid's chemically reacting biological convection mobility in conjunction with a gyrotactic microorganism and discontinuous radiant heat. The Reiner Philipp off motion of fluid was expanded by Gnaneswara Reddy et al. [34] in response to radiant energy. The impacts of heat radiation on 3-D circulation in convective barrier conditions in elasticity-sensitive liquids were intentional by Hayat et al. [35]. The influence of radiation and layer's level on the complex development of liquid-transporting aluminum dioxide and copper dioxide nanoparticles was examined by Wakif et al. [36]. Temperature properties of the Darcy-Forchheimer magnetohydrodynamic hybrid tiny fluid $(Al_2O_3 - Cu/H_2O)$ mobility was studied by Saeed et al. [37]. The double-dispersion thermally dynamics of elasticity-based nanomaterials was developed by Khan et al. [38] to account for energy absorption/production processes and the actual impacts of uneven radiant energy. The electronically radiated mobility of Williamson nanoliquid in a mixture of microorganisms was explored by Khan et al. [39]. In a square, clearly warmed room, Pop and Sheremet [40] explored the effects of viscous dispersion and thermal radiation on the Casson liquid free migration. Bhatti et al. [41] investigated the impacts of thermal irradiation across a Whirling sheet.

In the current model, heat generation/absorption, thermophoresis characteristics over a stretching surface, thermal radiation, Brownian motion, stagnation point, magnetic field, and thermophoresis are all included in the complicated model that includes Powell Eyring material. Using a boundary layer technique, the equations are first treated as partial expressions.

Following the developing of these partial differential equations (PDEs), the similarity approach is utilized to transform them into ordinary differential equations (ODEs), which are then computationally solved using the OHAM method.

2. ABBREVIATIONS AND ACRONYMS

u, v, w	velocity component	$\mathbb{x}, \mathbb{y}, \mathbb{z}$	coordinate axes
$\mathcal{D}_{\mathcal{B}}$	Brownian diffusion coefficient	ν	kinematic viscosity
$\mathcal{C}_f$	Skin friction coefficient	$\Bbbk$	Thermal conductivity
Nb	Brownian motion parameter	Nt	thermophoresis parameter
λ_t	relaxation time of heat flux	$\lambda_{\mathcal{C}}$	relaxation time of mass flux
a	constant parameter	$\mathcal{M}$	magnetic parameter
$\mathcal{T}$	temperature	$\mathcal{C}$	concentration
$\mathcal{T}_\infty$	ambient fluid temperature	$\mathcal{C}_\infty$	ambient fluid concentration
$\mathcal{T}_w$	surface temperature	$\mathcal{C}_w$	surface concentration
Rd	radiation parameter	f'	dimensionless velocity
θ	dimensionless temperature	φ	dimensionless concentration
Pr	Prandtl number	$\mathcal{B}_\circ$	magnetic field
δt	thermal relaxation parameter	δt	concentration relaxation parameter
$\mathcal{Sh}_{\mathbb{x}}$	local Sherwood number	$\mathcal{Re}_{\mathbb{x}}$	local Reynolds number

3. EQUATIONS

The steady, incompressible and viscous flow of Powell-Eyring nanofluid over a stretched sheet with two directions. In addition, the study takes into account nonlinear thermal radiation, Brownian motion, thermophoresis characteristics, a changeable heat generation/absorption and magnetic field terms. The selected coordinate system is oriented in the xy-plane, where the surface is stretched with stretching velocities $\mathbb{U}_{w}(\mathbb{x}) = a\mathbb{x}$ and $\mathcal{V}_{w}(\mathbb{y}) = b\mathbb{y}$ in both the x and $\mathbb{y}$ directions, as shown in Fig.1.where a and b stand for arbitrary constants. The fluid is permitted to rotate with a uniform angular velocity Ω about the z-axis while being regarded in the space $\mathbb{z} \geq 0$. The surface concentration of nanoparticles is represented by $\mathcal{C}_{w}$, while the ambient concentration is $\mathcal{C}_\infty$. For the analysis of heat transfer in this work, the non-Ficks mass flux theory and the non-Fourier heat flux theory are used.

The differential equations that follow, as used by Javed et al. [42], are obtained from the conservation laws of mass, energy and momentum, following boundary layer approximation.

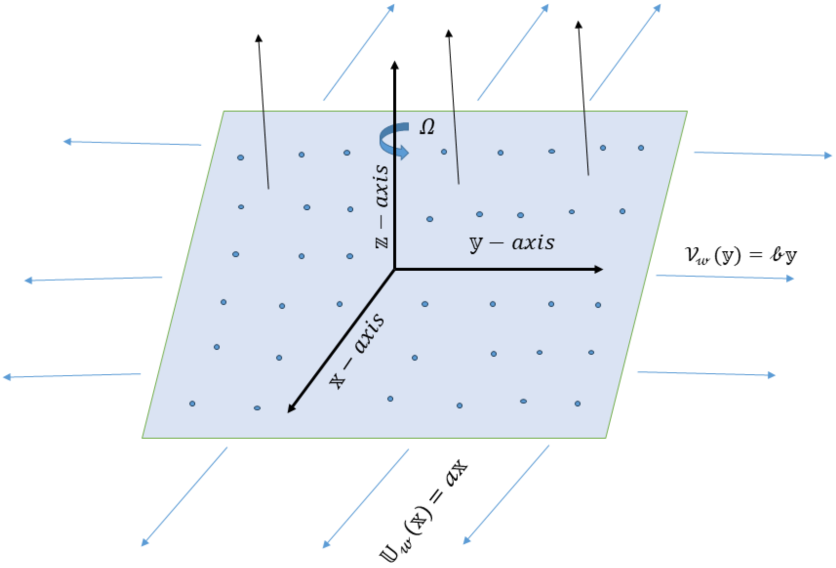

Fig. 1. Geometry of the problem.

$$\frac{\partial \bar{\bar{u}}}{\partial \mathbb{x}} + \frac{\partial \bar{\bar{v}}}{\partial \mathbb{y}} + \frac{\partial \bar{\bar{w}}}{\partial \mathbb{z}} = 0, \tag{1}$$

$$\bar{\bar{u}}\frac{\partial \bar{\bar{u}}}{\partial \mathbb{x}} + \bar{\bar{v}}\frac{\partial \bar{\bar{v}}}{\partial \mathbb{y}} + \bar{\bar{w}}\frac{\partial \bar{\bar{w}}}{\partial \mathbb{z}} - 2\Omega\bar{\bar{v}} = \left(\nu + \frac{1}{\rho\beta d}\right)\left(\frac{\partial^2 \bar{\bar{u}}}{\partial \mathbb{z}^2}\right) - \left(\frac{1}{2\rho\beta d^3}\right)\left(\frac{\partial \bar{\bar{u}}}{\partial \mathbb{z}}\right)^2\left(\frac{\partial^2 \bar{\bar{u}}}{\partial \mathbb{z}^2}\right) - \frac{\sigma\mathcal{B}_0^2}{\rho}\bar{\bar{u}}, \tag{2}$$

$$\bar{\bar{u}}\frac{\partial v}{\partial \mathbb{x}} + \bar{\bar{v}}\frac{\partial \bar{\bar{v}}}{\partial \mathbb{y}} + \bar{\bar{w}}\frac{\partial \bar{\bar{v}}}{\partial \mathbb{z}} - 2\Omega\bar{\bar{u}} = \left(\nu + \frac{1}{\rho\beta d}\right)\left(\frac{\partial^2 \bar{\bar{v}}}{\partial \mathbb{z}^2}\right) - \left(\frac{1}{2\rho\beta d^3}\right)\left(\frac{\partial \bar{\bar{v}}}{\partial \mathbb{z}}\right)^2\left(\frac{\partial^2 \bar{\bar{v}}}{\partial \mathbb{z}^2}\right) - \frac{\sigma\mathcal{B}_0^2}{\rho}\bar{\bar{v}}. \tag{3}$$

The following definitions apply to the enhanced mass diffusion and heat conduction expressions [44-45].

$$\hat{\mathbb{q}} + \lambda_t\left(\frac{\partial \hat{\mathbb{q}}}{\partial t} + V.\nabla\hat{\mathbb{q}} - \hat{\mathbb{q}}.\nabla V + (\nabla.V)\hat{\mathbb{q}}\right) = -\mathbb{k}\nabla t, \tag{4}$$

$$\hat{\mathbb{j}} + \lambda_{\mathcal{C}}\left(\frac{\partial \hat{\mathbb{j}}}{\partial t} + V.\nabla\hat{\mathbb{j}} - \hat{\mathbb{j}}.\nabla V + (\nabla.V)\hat{\mathbb{j}}\right) = -\mathcal{D}_{\mathcal{B}}\nabla\mathcal{C}. \tag{5}$$

The time lag needed to initiate heat flux after a temperature gradient is started is known as the thermal relaxation time, while the time lag needed to initiate mass flux after a concentration gradient is introduced at a certain point is known as the concentration relaxation time.

$$\begin{aligned}\bar{\bar{u}}\frac{\partial \mathcal{T}}{\partial \mathbb{x}} + \bar{\bar{v}}\frac{\partial \mathcal{T}}{\partial \mathbb{y}} + \bar{\bar{w}}\frac{\partial \mathcal{T}}{\partial \mathbb{z}} + \lambda_t\phi_t = \alpha\left(\frac{\partial^2 \mathcal{T}}{\partial \mathbb{z}^2}\right) + \tau\left\{\mathcal{D}_{\mathcal{B}}\left(\frac{\partial \mathcal{C}}{\partial \mathbb{z}}\frac{\partial \mathcal{T}}{\partial \mathbb{z}}\right) + \frac{\mathcal{D}_{\mathcal{T}}}{\mathcal{T}_\infty}\left[\left(\frac{\partial \mathcal{T}}{\partial \mathbb{z}}\right)^2\right]\right\}\\ + \frac{Q_0}{(\rho c)_f}(\mathcal{T} - \mathcal{T}_\infty) + \frac{16\delta^*\mathcal{T}_\infty^3}{3\tilde{m}(\rho c)_f}\frac{\partial^2 \mathcal{T}}{\partial \mathbb{z}^2},\end{aligned} \tag{6}$$

$$\bar{\bar{u}}\frac{\partial \mathcal{C}}{\partial \mathbb{x}} + \bar{\bar{v}}\frac{\partial \mathcal{C}}{\partial \mathbb{y}} + \bar{\bar{w}}\frac{\partial \mathcal{C}}{\partial \mathbb{z}} + \lambda_{\mathcal{C}}\phi_c = \mathcal{D}_{\mathcal{B}}\left(\frac{\partial^2 \mathcal{C}}{\partial \mathbb{z}^2}\right) + \frac{\mathcal{D}_{\mathcal{T}}}{\mathcal{T}_\infty}\left(\frac{\partial^2 \mathcal{T}}{\partial \mathbb{z}^2}\right). \tag{7}$$

The criteria for the boundaries are

$$\bar{\bar{u}} = \mathbb{U}_{w}(\mathbb{x}) = ax, \bar{\bar{v}} = \mathcal{V}_{w}(\mathbb{y}) = b\mathbb{y}, \bar{\bar{w}} = 0, \mathcal{T} = \mathcal{T}_{w},$$

$$\mathcal{D}_{\mathcal{B}} \frac{\partial \mathcal{C}}{\partial \mathbb{z}} + \frac{\mathcal{D}_{\mathcal{T}}}{\mathcal{T}_{\infty}} \frac{\partial \mathcal{T}}{\partial \mathbb{z}} = 0, at\ z = 0,$$

$$\bar{\bar{u}} \to 0, \bar{\bar{v}} \to 0, \mathcal{T} \to \mathcal{T}_{\infty}, \mathcal{C} \to \mathcal{C}_{\infty}\ as\ \mathbb{z} \to \infty. \tag{8}$$

Where,

$$\begin{aligned}\phi_{\mathcal{E}} = {} & \bar{\bar{u}}^2 \frac{\partial^2 \mathcal{T}}{\partial \mathbb{x}^2} + \bar{\bar{v}}^2 \frac{\partial^2 \mathcal{T}}{\partial \mathbb{y}^2} + \bar{\bar{w}}^2 \frac{\partial^2 \mathcal{T}}{\partial \mathbb{z}^2} + 2\bar{\bar{u}}\bar{\bar{v}} \frac{\partial^2 \mathcal{T}}{\partial \mathbb{x}\partial \mathbb{y}} + 2\,\bar{\bar{v}}\bar{\bar{w}} \frac{\partial^2 \mathcal{T}}{\partial \mathbb{y}\partial \mathbb{z}} + 2\bar{\bar{u}}\bar{\bar{w}} \frac{\partial^2 \mathcal{T}}{\partial \mathbb{x}\partial \mathbb{z}} \\ & + \left(\bar{\bar{u}} \frac{\partial \bar{\bar{u}}}{\partial \mathbb{x}} + \bar{\bar{v}} \frac{\partial \bar{\bar{u}}}{\partial \mathbb{y}} + \bar{\bar{w}} \frac{\partial \bar{\bar{u}}}{\partial \mathbb{z}}\right) \frac{\partial \mathcal{T}}{\partial \mathbb{x}} + \left(\bar{\bar{u}} \frac{\partial \bar{\bar{v}}}{\partial \mathbb{x}} + \bar{\bar{v}} \frac{\partial \bar{\bar{v}}}{\partial \mathbb{y}} + \bar{\bar{w}} \frac{\partial \bar{\bar{v}}}{\partial \mathbb{z}}\right) \frac{\partial \mathcal{T}}{\partial \mathbb{y}} \\ & + \left(\bar{\bar{u}} \frac{\partial \bar{\bar{w}}}{\partial \mathbb{x}} + \bar{\bar{v}} \frac{\partial \bar{\bar{w}}}{\partial \mathbb{y}} + \bar{\bar{w}} \frac{\partial \bar{\bar{w}}}{\partial \mathbb{z}}\right) \frac{\partial \mathcal{T}}{\partial \mathbb{z}},\end{aligned} \tag{9}$$

$$\begin{aligned}\phi_{c} = {} & \bar{\bar{u}}^2 \frac{\partial^2 \mathcal{C}}{\partial \mathbb{x}^2} + \bar{\bar{v}}^2 \frac{\partial^2 \mathcal{C}}{\partial \mathbb{y}^2} + \bar{\bar{w}}^2 \frac{\partial^2 \mathcal{C}}{\partial \mathbb{z}^2} + 2\bar{\bar{u}}\bar{\bar{v}} \frac{\partial^2 \mathcal{C}}{\partial \mathbb{x}\partial \mathbb{y}} + 2\bar{\bar{v}}\bar{\bar{w}} \frac{\partial^2 \mathcal{C}}{\partial \mathbb{y}\partial \mathbb{z}} + 2\bar{\bar{u}}\bar{\bar{w}} \frac{\partial^2 \mathcal{C}}{\partial \mathbb{x}\partial \mathbb{z}} \\ & + \left(\bar{\bar{u}} \frac{\partial \bar{\bar{u}}}{\partial \mathbb{x}} + \bar{\bar{v}} \frac{\partial \bar{\bar{u}}}{\partial \mathbb{y}} + \bar{\bar{w}} \frac{\partial \bar{\bar{u}}}{\partial \mathbb{z}}\right) \frac{\partial \mathcal{C}}{\partial \mathbb{x}} + \left(\bar{\bar{u}} \frac{\partial \bar{\bar{v}}}{\partial \mathbb{x}} + \bar{\bar{v}} \frac{\partial \bar{\bar{v}}}{\partial \mathbb{y}} + \bar{\bar{w}} \frac{\partial \bar{\bar{v}}}{\partial \mathbb{z}}\right) \frac{\partial \mathcal{C}}{\partial \mathbb{y}} \\ & + \left(\bar{\bar{u}} \frac{\partial \bar{\bar{w}}}{\partial \mathbb{x}} + \bar{\bar{v}} \frac{\partial \bar{\bar{w}}}{\partial \mathbb{y}} + \bar{\bar{w}} \frac{\partial \bar{\bar{w}}}{\partial \mathbb{z}}\right) \frac{\partial \mathcal{C}}{\partial \mathbb{z}}.\end{aligned} \tag{10}$$

Selecting the subsequent transformations

$$\bar{\bar{u}} = a\mathbb{x}f'(\zeta), \bar{\bar{v}} = a\mathbb{y}g'(\zeta), \bar{\bar{w}} = -\sqrt{a\nu}\big(f(\zeta) + g(\zeta)\big),$$

$$\theta(\zeta) = \frac{\mathcal{T} - \mathcal{T}_{\infty}}{\mathcal{T}_{w} - \mathcal{T}_{\infty}}, \phi(\eta) = \frac{\mathcal{C} - \mathcal{C}_{\infty}}{\mathcal{C}_{w} - \mathcal{C}_{\infty}}, \zeta = \sqrt{\frac{a}{\nu}}z. \tag{11}$$

The verification of the continuity equation is equivalent, and the equations pertaining to momentum, energy, and concentration are simplified to.

$$(1 + S)f''' - S\mathbb{k}1(f'')^2 f''' - (f')^2 + (f + g)f'' + 2\lambda B g' - \mathcal{M}f' = 0, \tag{12}$$

$$(1 + S)g''' - S\mathbb{k}2(g'')^2 g''' - (g')^2 + (f + g)g'' + 2\frac{\lambda}{B}f' - \mathcal{M}g' = 0, \tag{13}$$

$$\begin{aligned}&(1 + Rd)\theta'' + \Pr(Nb\theta'\phi' + Nt(\theta')^2 + (f + g)\theta' \\ &\qquad -\delta t[(f + g)(f' + g')\theta' + (f + g)^2\theta''] + \delta_{hg}\theta) = 0,\end{aligned} \tag{14}$$

$$\phi'' + \frac{Nt}{Nb}\theta'' + Sc\big((f + g)\phi' - \delta c(f + g)(f' + g')\phi' + (f + g)^2\phi''\big) = 0. \tag{15}$$

The requirements for the boundaries are.

$$f(0) = 0, f'(0) = 1, g(0) = 0, g'(0) = A, \theta(0) = 1, \phi(0) = 1, \text{at } \zeta = 0,$$

$$f'(\infty) \to 0, g'(\infty) \to 0, \theta(\infty) \to 0, \phi(\infty) \to 0, \text{as } \zeta \to \infty. \tag{16}$$

The following lists the mathematical formulations for the dimensionless parameters connected to Eqs. (12-16).

Where $A = \frac{\mathscr{b}}{a}, \lambda = \frac{\Omega}{a}, B = \frac{\mathbb{y}}{\mathbb{x}}, S = \frac{1}{\mu\beta d}, \mathbb{k}1 = \frac{a^3\mathbb{x}^2}{2\nu d^2}, \mathbb{k}2 = \frac{a^3\mathbb{y}^2}{2\nu d^2}, \mathcal{M} = \frac{\sigma\mathcal{B}_0^2}{\rho a}, Pr = \frac{\nu}{\alpha}, Sc = \frac{\nu}{\mathcal{D}_{\mathcal{B}}}, Nb = \frac{\tau\mathcal{D}_{\mathcal{B}}\mathcal{C}_\infty}{\nu}, Nt = \frac{\tau\mathcal{D}_{\mathcal{T}}}{\nu\mathcal{T}_\infty}(\mathcal{T}_w - \mathcal{T}_\infty), \delta t = \lambda_t a, \delta_c = \lambda_{\mathcal{C}} a, \delta_{hg} = \frac{\mathcal{Q}}{(\rho c)_f a}$, and $Rd = \frac{16\delta^*\mathcal{T}_\infty^3}{3\tilde{m}a}$. (17)

The Skin friction $\mathcal{C}_{f\mathbb{x}}$ Sherwood number $\mathcal{S}\hbar_{\mathbb{x}}$ and local Nusselt number $\mathcal{N}u_{\mathbb{x}}$, formulae are provided below:

$$\mathcal{C}_{f\mathbb{x}} = \frac{\tau_{w\mathbb{x}}}{\rho(\mathbb{U}_w)^2}, \mathcal{C}_{f\mathbb{y}} = \frac{\tau_{w\mathbb{y}}}{\rho(\mathcal{V}_w)^2}, \mathcal{N}u_{\mathbb{x}} = \frac{\mathbb{x}q_w}{\mathbb{k}(\mathcal{T}_w - \mathcal{T}_\infty)}, \mathcal{S}\hbar_{\mathbb{x}} = \frac{\mathbb{x}\hbar_w}{\mathcal{D}_{\mathcal{B}}(\mathcal{C}_w - \mathcal{C}_\infty)}. \tag{18}$$

$\mathbb{q}_w$ and $\hbar_w$ are defined as follows, where $\tau_{w\mathbb{x}}$ and $\tau_{w\mathbb{y}}$ are the wall shear stress along the $\mathbb{x}$ and $\mathbb{y}$ axes:

$$\tau_{w\mathbb{x}} = \mu\left(\frac{\partial\bar{\bar{u}}}{\partial z} + \frac{\partial\bar{\bar{w}}}{\partial\mathbb{x}}\right)_{z=0}, \tau_{w\mathbb{y}} = \mu\left(\frac{\partial\bar{\bar{v}}}{\partial z} + \frac{\partial\bar{\bar{w}}}{\partial\mathbb{y}}\right)_{z=0}, \mathbb{q}_w = -\mathbb{k}\left(\frac{\partial\mathcal{T}}{\partial z}\right)_{z=0}, \quad \hbar_w = -\mathcal{D}_{\mathcal{B}}\left(\frac{\partial\mathcal{C}}{\partial z}\right)_{z=0}. \tag{19}$$

Equations above give us

$$\mathcal{C}_{f\mathbb{x}}\,(\mathcal{R}e_{\mathbb{x}})^{\frac{1}{2}} = (1+S)f''(0) - \frac{1}{3}S\mathbb{k}1(f''')^3(0),$$

$$\mathcal{C}_{f\mathbb{y}}\left(\mathcal{R}e_{\mathbb{y}}\right)^{\frac{1}{2}} = (1+S)g''(0) - \frac{1}{3}S\mathbb{k}2(g''')^3(0),$$

$$\frac{\mathcal{N}u_{\mathbb{x}}}{(\mathcal{R}e_{\mathbb{x}})^{\frac{1}{2}}} = -\theta'(0), \frac{\mathcal{S}\hbar_{\mathbb{x}}}{(\mathcal{R}e_{\mathbb{x}})^{\frac{1}{2}}} = -\phi'(0). \tag{20}$$

where the local Reynolds numbers are $\mathcal{R}e_{\mathbb{x}}$ and $\mathcal{R}e_{\mathbb{y}}$.

Solution by OHAM

Convergent homotopic solutions are created by applying the optimum homotopy analysis approach (OHAM). Linear auxiliary machinists $(\grave{\mathcal{L}}(f), \grave{\mathcal{L}}(g), \grave{\mathcal{L}}(\theta), \grave{\mathcal{L}}(\phi))$ and the suitable initial estimates $(f_0(\zeta), g_0(\zeta), \theta_0(\zeta), \phi_0(\zeta))$ for homotopic solutions are defined as follows:

$$f_0(\zeta) = 1 - e^{-\zeta}, g_0(\zeta) = A(1 - e^{-\zeta})$$

$$\theta_0(\zeta) = e^{-\zeta}, \phi_0(\zeta) = e^{-\zeta},$$

$$\tilde{\mathcal{L}}(f) = f''' - f', \tilde{\mathcal{L}}(g) = g''' - g',$$

$$\tilde{\mathcal{L}}(\theta) = \theta'' - \theta, \tilde{\mathcal{L}}(\phi) = \phi'' - \phi. \tag{21}$$

The above linear operators satisfy the following properties.

$$\tilde{\mathcal{L}}(f)[j_1 + j_2 e^{-\zeta} + j_3 e^{-\zeta}] = 0,$$

$$\tilde{\mathcal{L}}(g)[j_4 + j_5 e^{-\zeta} + j_6 e^{-\zeta}] = 0,$$

$$\tilde{\mathcal{L}}(\theta)[j_7 e^{-\zeta} + j_8 e^{-\zeta}] = 0,$$

$$\tilde{\mathcal{L}}(\phi)[j_9 e^{-\zeta} + j_{10} e^{-\zeta}] = 0. \tag{22}$$

where the random constants are represented by $j_n(n = 1\ to\ 10)$.

Convergence analysis

As suggested by Liao, we have utilized the idea of minimization to represent the average squared residual errors in order to ascertain the optimal values of $\ddot{\mathfrak{h}}(f)$, $\ddot{\mathfrak{h}}(g)$, $\ddot{\mathfrak{h}}(\theta)$, and $\ddot{\mathfrak{h}}(\phi)$. In approximation homotopic solutions, the convergence zone and rate of homotopic solutions are governed by the non-zero convergence control parameters $\ddot{\mathfrak{h}}(f)$, $\ddot{\mathfrak{h}}(g)$, $\ddot{\mathfrak{h}}(\theta)$, and $\ddot{\mathfrak{h}}(\phi)$.

$$\epsilon_m(f) = \frac{1}{\mathbb{k}+1}\sum_{n=0}^{l}[\breve{\mathcal{N}}(f)(\sum_{i=0}^{m}\tilde{f}(\zeta), \sum_{i=0}^{m}\tilde{g}(\zeta))_{\zeta=n\delta\zeta}]^2, \tag{23}$$

$$\epsilon_m(g) = \frac{1}{\mathbb{k}+1}\sum_{n=0}^{l}[\breve{\mathcal{N}}(g)(\sum_{i=0}^{m}\tilde{f}(\zeta),\sum_{i=0}^{m}\tilde{g}(\zeta))_{\zeta=n\delta\zeta}]^2, \tag{24}$$

$$\epsilon_m(\theta) = \frac{1}{\mathbb{k}+1}\sum_{n=0}^{l}[\breve{\mathcal{N}}(\theta)(\sum_{i=0}^{m}\tilde{f}(\zeta),\sum_{i=0}^{m}\tilde{g}(\zeta),\sum_{i=0}^{m}\tilde{\theta}(\zeta),\sum_{i=0}^{m}\tilde{\phi}(\zeta))_{\zeta=n\delta\zeta}]^2, \tag{25}$$

$$\epsilon_m(\phi) = \frac{1}{\mathbb{k}+1}\sum_{n=0}^{l}[\breve{\mathcal{N}}(\phi)(\sum_{i=0}^{m}\tilde{f}(\zeta),\sum_{i=0}^{m}\tilde{g}(\zeta),\sum_{i=0}^{m}\tilde{\theta}(\zeta),\sum_{i=0}^{m}\tilde{\phi}(\zeta))_{\zeta=n\delta\zeta}]^2. \tag{26}$$

Following Liao [43]

$$\epsilon_m t = \epsilon_m(f) + \epsilon_m(g) + \epsilon_m(\theta) + \epsilon_m(\phi). \tag{27}$$

In this case, $\mathbb{K}$=20 and $\delta\zeta = 0.5$., and $\epsilon_m t$ indicates the residual error's total average squared. The residual error's total average squared was reduced with Mathematica BVPh2.0. An example using $A = \lambda = Rd = 0.1$, $\delta t = \delta c = B = \mathcal{M} = k2 = 0.2$, $\mathbb{k}1 = Nt = Nb = 0.3$, $\delta = 0.4$, $S = 0.5$ and $Sc = Pr = 1.1$ has been examined. At second order of approximations, the ideal convergence control parameter values are:

4. FIGURES AND TABLES

Table I. USE OF IDEAL VALUES FROM AUXILIARY PARAMETERS TO OBTAIN INDIVIDUAL AVERAGED SQUARED RESIDUAL ERRORS

m	$\epsilon_m(f)$	$\epsilon_m(g)$	$\epsilon_m(\theta)$	$\epsilon_m(\phi)$
2	2.2759×10^{-4}	5.59842×10^{-3}	1.77326×10^{-2}	1.307072×10^{-2}
4	1.36533×10^{-4}	3.16667×10^{-3}	1.02721×10^{-2}	6.02523×10^{-3}
6	1.00293×10^{-4}	2.31082×10^{-3}	7.91089×10^{-3}	4.71982×10^{-3}
8	8.41674×10^{-5}	1.87956×10^{-3}	6.8099×10^{-3}	4.25449×10^{-3}
10	7.20903×10^{-5}	1.62282×10^{-3}	6.22386×10^{-3}	4.03337×10^{-3}
12	6.36668×10^{-5}	1.45431×10^{-3}	5.90109×10^{-3}	3.90935×10^{-3}
14	5.74671×10^{-5}	1.33655×10^{-3}	5.73265×10^{-3}	3.83463×10^{-3}
16	5.27244×10^{-5}	1.25007×10^{-3}	5.66381×10^{-3}	3.79001×10^{-3}
18	4.89893×10^{-5}	1.18625×10^{-3}	5.55425×10^{-3}	3.61658×10^{-3}
20	4.05981×10^{-5}	1.13689×10^{-3}	5.21589×10^{-3}	3.34894×10^{-3}

Analyzing the achievements of governing parameters on the temperature, concentration profiles, and flow field is the goal of this section.

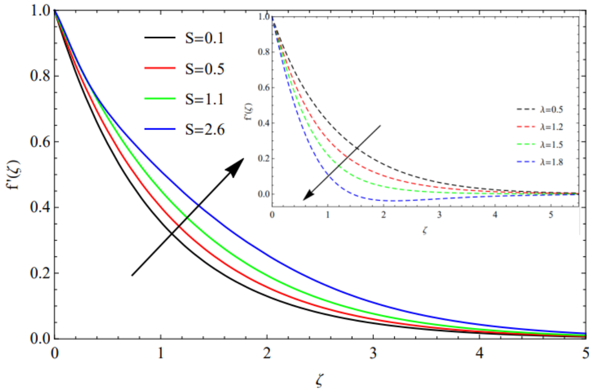

Fig. 2. Encouragement of λ and S on $f'(\zeta)$.

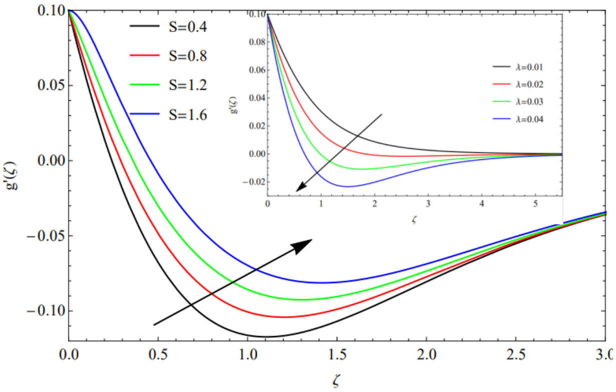

Fig. 3. Encouragement of λ and S on $g'(\zeta)$.

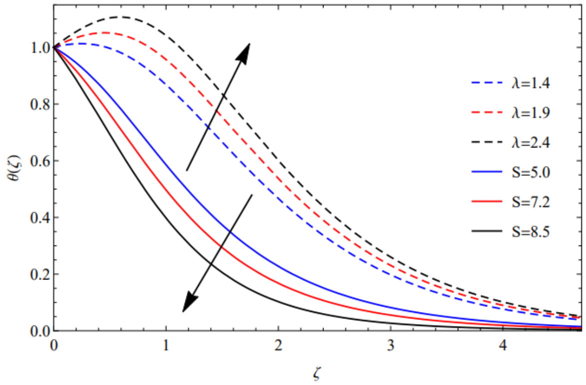

Fig. 4. Encouragement of λ and S on $\theta(\zeta)$.

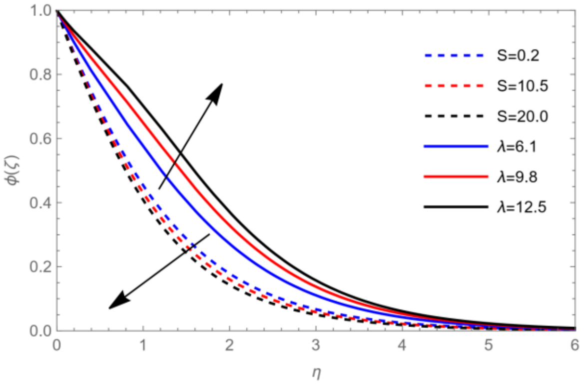

Fig. 5. Encouragement of λ and S on $\phi(\zeta)$.

The influence of rotation parameter λ and non-Newtonian parameter S on non-dimensional velocity across the $\mathbb{x}$ -direction is depicted in Fig. 1. While the rotation parameter functions in the reverse way, the non-Newtonian parameter S acts as an inducer of a velocity boundary layer thickness increment. The rotation parameter physically lowers the fluid's linear velocity because of the flow's rotating friction force, decreases the fluid's velocity while it is spinning and flowing. Fig. 2 displays the velocity curve along the $\mathbb{y}$-direction. Because the velocity boundary layer thickness along the $\mathbb{y}$ -direction reduced as the rotation parameter λ grows, the fluid is spinning. When the non-Newtonian parameter S rises, the $\mathbb{y}$ -direction velocity also rises. Fig. 3 illustrates that temperature rises with increasing rotation parameter λ. When the fluid is Newtonian, the temperature variation is larger. In contrast, the non-Newtonian parameter S behaves in the other way. Fig. 4 illustrates how the concentration boundary layer thickness grows with a rise in the rotation parameter λ. The boundary layer thickness decreases with a decrease in the degree of non-Newtonian parameter S.

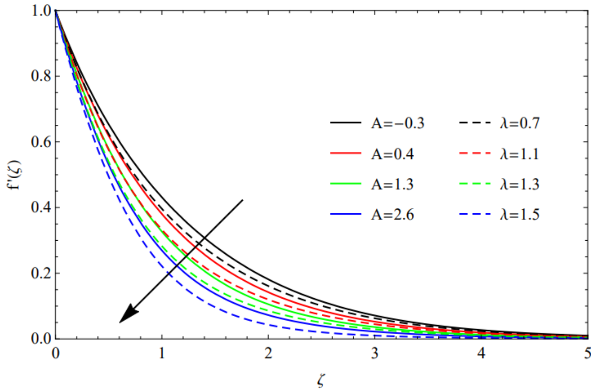

Fig. 6. Encouragement of λ and A on $f'(\zeta)$.

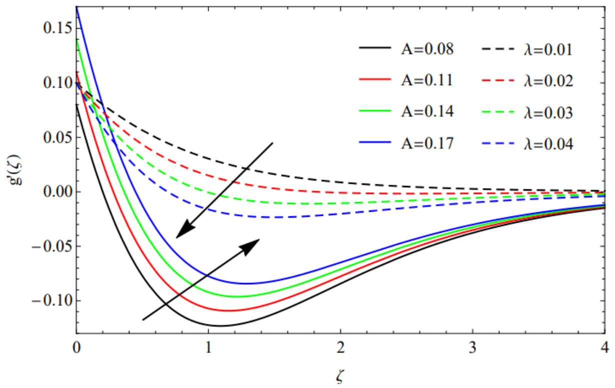

Fig. 7. Encouragement of λ and A on $g'(\zeta)$.

Fig. 5 illustrates that an escalation in the values of A and rotation parameter λ corresponds to the velocity profile's decrease. Fig 6 scrutinizes the effect of augmenting the rotation parameter λ on the velocity boundary layer thickness along the $\mathbb{y}$-direction, indicating a reduction. Conversely, elevating the values of A leads to an increase in the velocity boundary layer thickness along the $\mathbb{y}$-direction.

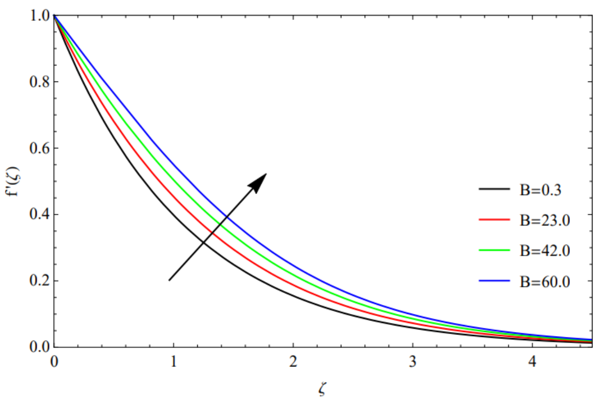

Fig. 8. Encouragement of B on $f'(\zeta)$.

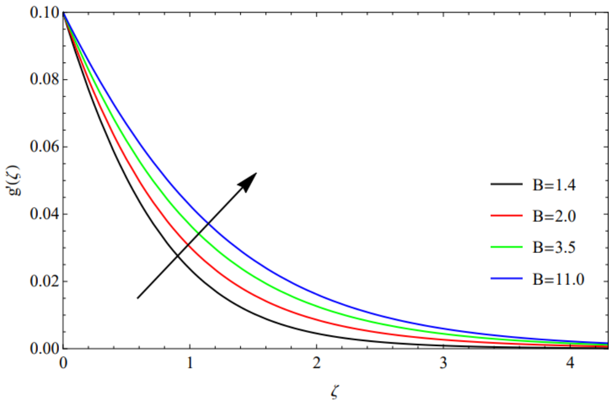

Fig. 9. Encouragement of B on $g'(\zeta)$.

Fig. 7 and 8 delineate velocity profiles along the $\mathbb{x}$ and $\mathbb{y}$ -axes. The observed trend is such that as the values of the rotation factor B escalate, both dimensionless velocities across the $\mathbb{x}$ and $\mathbb{y}$-axes exhibit an ascending behavior.

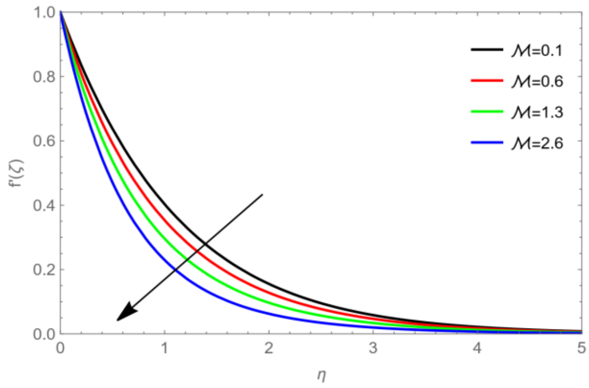

Fig. 10. Encouragement of M on $f'(\zeta)$.

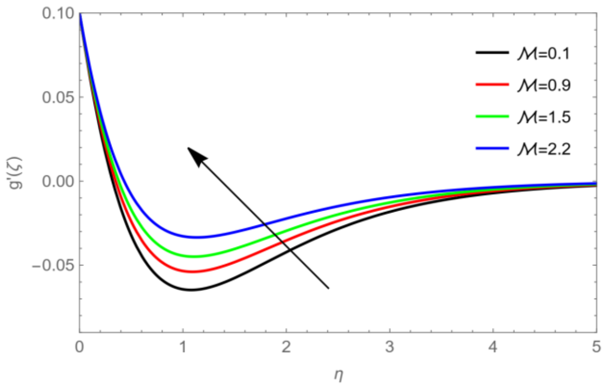

Fig. 11. Encouragement of M on $g'(\zeta)$.

Figure 9 illustrates how the velocity profile along the $\mathbb{x}$-axis decreases as the magnetic field intensity values rise, whereas Figure 10 displays the opposite behavior along the $\mathbb{y}$-axis.

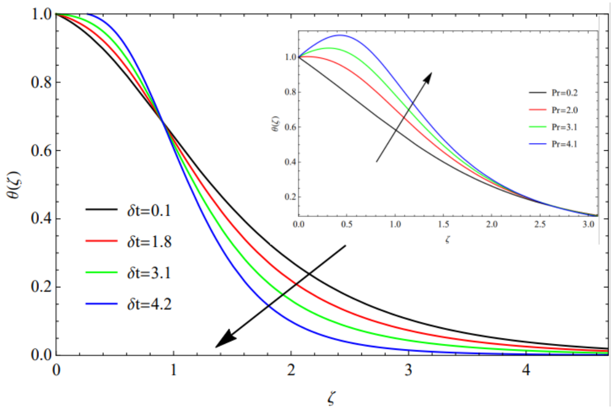

Fig. 12. Encouragement of Pr and δt on $\theta(\zeta)$.

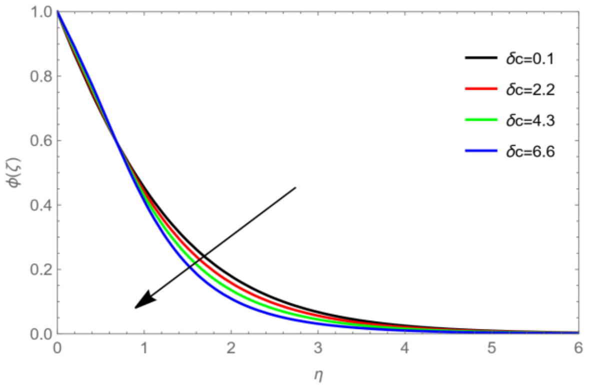

Fig. 13. Encouragement of δ_c on $\phi(\zeta)$.

Fig. 11 shows how the temperature graph changes as the Pr and time relaxation parameter δt rises. The heat transfer increases but the thickness of the thermal boundary layer decreases as the time relaxation parameter δt grows. As the Pr rises, the thickness of the thermal boundary layer rises. The thickness of the concentration boundary layer falls as the concentration relaxation factor δc increases, as shown in Fig. 12.

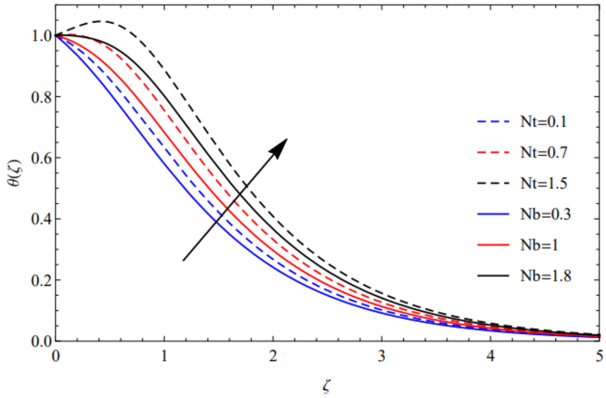

Fig. 14. Encouragement of Nt and Nb on $\theta(\zeta)$.

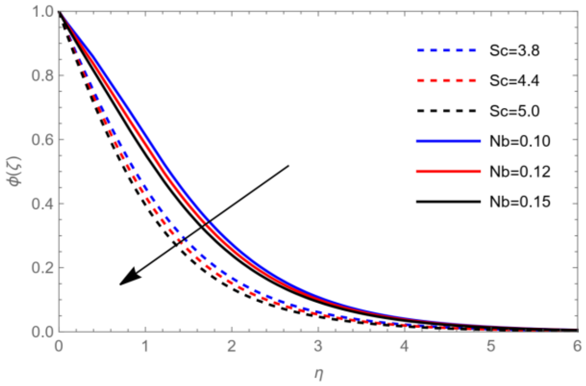

Fig. 15. Encouragement of Sc and Nb on $\phi(\zeta)$.

The behavior of Nb. and Nt on the temperature profile is portrayed in Fig. 13. The thickness of the thermal boundary layer grows together with the values of the thermophoresis parameter Nt and Nb. The concentration graph with the Schmidt number Sc and Nb are displayed in Fig. 14. The concentration boundary layer thickness falls with growing values of both parameters.

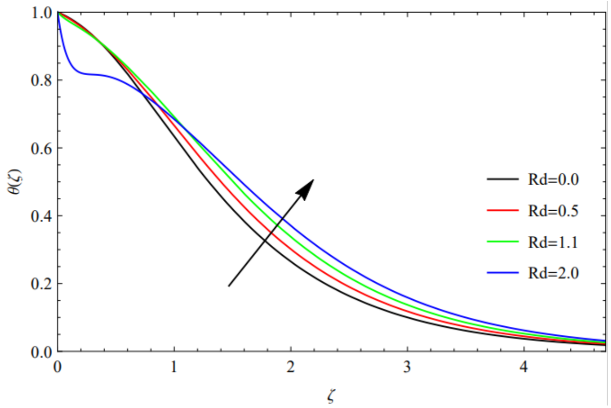

Fig. 16. Encouragement of Rd on $\theta(\zeta)$.

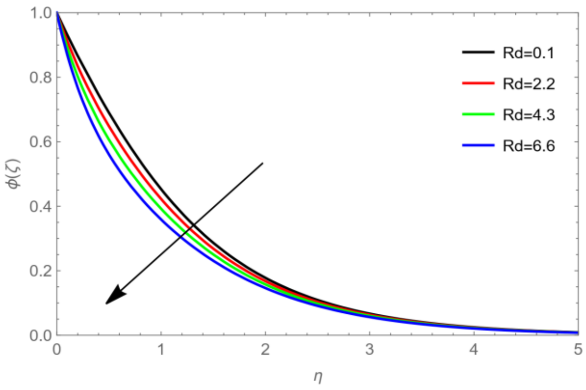

Fig. 17. Encouragement of Rd on $\phi(\zeta)$.

As the values of Rd rise, the thermal profile and thermal boundary layer likewise rise, as illustrated in Fig. 15. As the radiation parameter Rd rises, the concentration profile and the thickness of the concentration boundary layer reduce, as Fig. 16 illustrates.

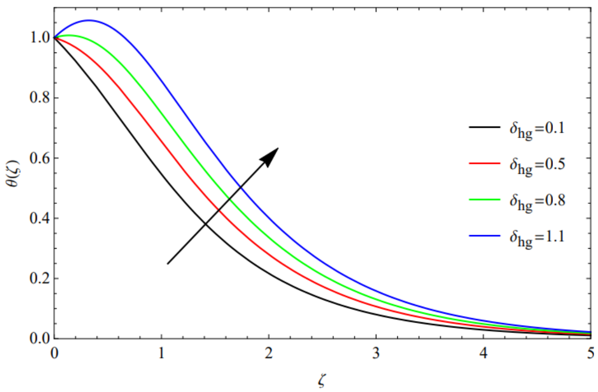

Fig. 18. Encouragement of δ_{hg} on $\theta(\zeta)$.

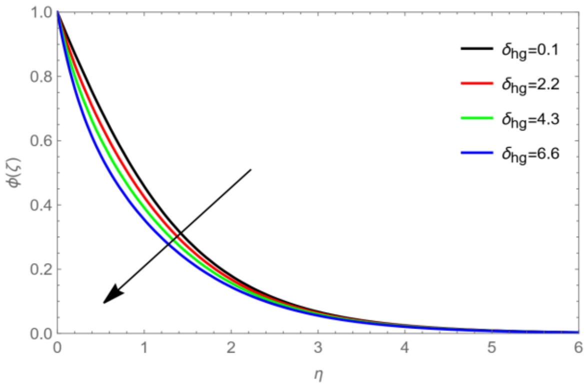

Fig. 19. Encouragement of δ_{hg} on $\phi(\zeta)$.

Fig. 17 illustrates that the concentration boundary layers and thickness of the thermal grows together with the magnitude of the heat generation parameter δ_{hg}. Fig. 18 illustrates that the concentration boundary layers and thickness of the thermal only lowers when the value of the heat generation parameter δ_{hg} rises.

TABLE II. THE CALCULATED VALUES OF $f''(0)$ WITH VARYING S, λ, and B.

S	λ	B	$f''(0)$
0.001	0.1	0.1	−1.09697
0.004	0.1	0.1	−1.09926
0.006	0.1	0.1	−1.10078
0.008	0.1	0.1	−1.1023
0.01	0.2	0.1	−1.09406
0.01	0.3	0.1	−1.0866
0.01	0.4	0.1	−1.08145
0.01	0.5	0.1	−1.07858
0.01	0.1	0.07	−1.05786
0.01	0.1	0.09	−1.06116
0.01	0.1	0.1	−1.06226
0.01	0.1	0.2	−1.06644

TABLE III. CALCULATED VALUES OF $g''(0)$ FOR VARIOUS for S, A, AND $\mathcal{M}$ VALUES.

S	A	$\mathcal{M}$	$g''(0)$
0.1	0.1	0.2	-0.575664
0.2	0.1	0.2	−0.605556
0.3	0.1	0.2	−0.633425
0.4	0.1	0.2	−0.659807
0.1	0.1	0.2	−0.308672
0.1	0.1	0.2	−0.403058
0.1	0.1	0.2	−0.506511
0.1	0.1	0.2	−0.618906
0.1	02	0.1	−0.854537
0.1	0.2	0.2	−0.871939
0.1	0.2	0.3	−0.889119
0.1	0.2	0.4	−0.906079

TABLE IV. THE VALUES OF $-\theta'(0)$ FOR VARIOUS PHYSICAL PARAMETER VALUES

λ	S	δt	Pr	Nt	Nb	δ_{hg}	$-\theta'(0)$
0.6	0.3	0.4	0.8	0.2	0.1	0.3	0.452279
0.7	0.3	0.4	0.8	0.2	0.1	0.3	0.44915
0.8	0.3	0.4	0.8	0.2	0.1	0.3	0.446021
0.9	0.3	0.4	0.8	0.2	0.1	0.3	0.443245
0.9	0.4	0.4	0.8	0.2	0.1	0.3	0.443599
0.9	0.5	0.4	0.8	0.2	0.1	0.3	0.443952
0.9	0.6	0.5	0.8	0.2	0.1	0.3	0.444337

0.9	0.7	0.6	0.8	0.2	0.1	0.3	0.444360
0.9	0.7	0.7	0.8	0.2	0.1	0.3	0.444363
0.9	0.7	0.8	0.9	0.2	0.1	0.3	0.436131
0.9	0.7	0.8	1.0	0.2	0.1	0.3	0.427961
0.9	0.7	0.8	1.1	0.2	0.1	0.3	0.419848
0.9	0.7	0.8	1.2	0.3	0.2	0.3	0.401193
0.9	0.7	0.8	1.2	0.4	0.3	0.3	0.392297
0.9	0.7	0.8	1.2	0.5	0.4	0.3	0.385105
0.9	0.7	0.8	1.2	0.6	0.5	0.3	0.364256
0.9	0.7	0.8	1.2	0.6	0.5	0.3	0.349745
0.9	0.7	0.8	1.2	0.6	0.5	0.3	0.336087
0.9	0.7	0.8	1.2	0.6	0.5	0.4	0.280695
0.9	0.7	0.8	1.2	0.6	0.5	0.5	0.237353
0.9	0.7	0.8	1.2	0.6	0.5	0.6	0.193251

TABLE V. IMPACT OF S, A, Sc, Nb,Rd AND δ_{hg} on $-\phi'(0)$.

S	λ	Sc	Nb	Rd	δ_{hg}	$-\phi'(0)$
0.3	0.4	0.2	0.4	0.6	0.1	0.683124
0.4	0.4	0.2	0.4	0.6	0.1	0.683178
0.5	0.4	0.2	0.4	0.6	0.1	0.683231
0.6	0.4	0.2	0.4	0.6	0.1	0.683284
0.6	0.5	0.2	0.4	0.6	0.1	0.682813
0.6	0.6	0.2	0.4	0.6	0.1	0.682342
0.6	0.7	0.2	0.4	0.6	0.1	0.681872
0.6	0.8	0.2	0.4	0.6	0.1	0.681401
0.6	0.8	0.3	0.4	0.6	0.1	0.687539
0.6	0.8	0.4	0.4	0.6	0.1	0.693708
0.6	0.8	0.5	0.4	0.6	0.1	0.699907
0.6	0.8	0.6	0.4	0.6	0.1	0.712398
0.6	0.8	0.6	0.5	0.6	0.1	0.725612
0.6	0.8	0.6	0.6	0.6	0.1	0.73442
0.6	0.8	0.6	0.7	0.6	0.1	0.740712
0.6	0.8	0.6	0.8	0.6	0.1	0.745431
0.6	0.8	0.6	0.8	0.7	0.1	0.749868
0.6	0.8	0.6	0.8	0.8	0.1	0.754304
0.6	0.8	0.6	0.8	0.9	0.1	0.75874
0.6	0.8	0.6	0.8	1.0	0.1	0.763177
0.6	0.8	0.6	0.8	1.0	0.1	0.768057
0.6	0.8	0.6	0.8	1.0	0.1	0.772937
0.6	0.8	0.6	0.8	1.0	0.1	0.77781
0.6	0.8	0.6	0.8	1.0	0.1	0.782697

Individual average squared residual errors are shown in Table 1 based on optimal convergence control parameter data at $m = 2$. It is evident that with higher order deformations, the averaged squared residual error diminishes. Tables 2, 3, 4, and 5 present the numerical values of the skin friction coefficient, Nusselt number, and Sherwood number across varied flow parameter values.

CONCLUSION

This research provides a computational investigate of the Powell-Eyring nanofluid in rotational motion across a bidirectional stretching surface. A thorough examination of heat transfer processes is achieved with the application of the Cattaneo-Christov heat flux model. The study's key findings include the following:

1. One notable property of the rotational parameter (λ) is its capacity to decrease the hydrodynamic boundary layer thickness:

   At the same time, the boundary layer's heat transfer is reduced by the rotational parameter (λ);

   1. In Newtonian fluids, the effect of the rotational parameter (λ) is larger than in their non-Newtonian counterparts;
   2. The thermal boundary layer's thickness is effectively reduced by the thermal relaxation parameter (δ_t);
   3. The concentration profile is influenced similarly by the concentration parameter δ_c and the thermal relaxation parameter (δ_t);
   4. The local Nusselt number is driven by the time relaxation parameter δ_t which includes radiation, heat production, magnetohydrodynamics (MHD), and the Optimal Homotopy Analysis Method

   On both the $\mathbb{x}$ and $\mathbb{y}$ axes, the non-Newtonian parameter (S) causes the skin friction coefficient to decrease.

Funding

The acknowledgments section of the paper does not mention any financial support from institutions or sponsors.

Conflicts of of interest

The author's paper declares that there are no relationships or affiliations that could create conflicts of interest.

Acknowledgment

The author acknowledges the institution for the intellectual resources and academic guidance that significantly enriched this research.

References

[1] Chakraborty, S. and Panigrahi, P.K., 2020. Stability of nanofluid: A review. *Applied Thermal Engineering*, *174*, p.115259.

[2] Ibrahim, W. and Shankar, B., 2013. MHD boundary layer flow and heat transfer of a nanofluid past a permeable stretching sheet with velocity, thermal and solutal slip boundary conditions. *Computers & Fluids*, *75*, pp.1-10.

[3] Sabir, Z., Akhtar, R., Zhiyu, Z., Umar, M., Imran, A., Wahab, H.A., Shoaib, M. and Raja, M.A.Z., 2019. A computational analysis of two-phase casson nanofluid passing a stretching sheet using chemical reactions and gyrotactic microorganisms. *Mathematical Problems in Engineering*, *2019*.

[4] Sheremet, M. A., Grosan, T., & Pop, I. (2015). Steady-state free convection in right-angle porous trapezoidal cavity filled by a nanofluid: Buongiorno's mathematical model. *European Journal of Mechanics-B/Fluids*, *53*, 241-250.

[5] Niihara, K. (1991). New design concept of structural ceramics ceramic nanocomposites. *Journal of the Ceramic Society of Japan*, *99*(1154), 974-982.

[6] Asirvatham, L. G., Vishal, N., Gangatharan, S. K., & Lal, D. M. (2009). Experimental study on forced convective heat transfer with low volume fraction of CuO/water nanofluid. *Energies*, *2*(1), 97-119.

[7] Mittal, N., Manoj, V., Kumar, D. S., & Satheesh, A. (2013). Numerical simulation of mixed convection in a porous medium filled with water/Al_2O_3 nanofluid. *Heat Transfer—Asian Research*, *42*(1), 46-59.

[8] Akbar, N.S., Ebaid, A. and Khan, Z.H., 2015. Numerical analysis of magnetic field effects on Eyring-Powell fluid flow towards a stretching sheet. *Journal of magnetism and Magnetic Materials*, *382*, pp.355-358.

[9] Mustafa, T., 2020. Eyring–Powell fluid flow through a circular pipe and heat transfer: full solutions. *International Journal of Numerical Methods for Heat & Fluid Flow*, *30*(11), pp.4765-4774.

[10] Sumithra, A., Sivaraj, R., Benazir, A.J. and Makinde, O.D., 2021. Nonlinear thermal radiation and activation energy effects on bioconvective flow of Eyring-Powell fluid. *Computational Thermal Sciences: An International Journal*, *13*(6).

[11] Umar, M., Akhtar, R., Sabir, Z., Wahab, H.A., Zhiyu, Z., Imran, A., Shoaib, M. and Raja, M.A.Z., 2019. Numerical treatment for the three-dimensional Eyring-Powell fluid flow over a stretching sheet with velocity slip and activation energy. *Advances in Mathematical Physics*, *2019*, pp.1-12.

[12] Nadeem, S., Akbar, N.S. and Ali, M., 2012. Endoscopic effects on the peristaltic flow of an Eyring–Powell fluid. *Meccanica*, *47*, pp.687-697.

[13] Hayat, T., Iqbal, Z., Qasim, M. and Obaidat, S., 2012. Steady flow of an Eyring Powell fluid over a moving surface with convective boundary conditions. *International Journal of Heat and Mass Transfer*, *55*(7-8), pp.1817-1822.

[14] Nadeem, S. and Saleem, S., 2014. Mixed convection flow of Eyring–Powell fluid along a rotating cone. *Results in Physics*, *4*, pp.54-62.

[15] Seyedi, S.H., Saray, B.N. and Chamkha, A.J., 2020. Heat and mass transfer investigation of MHD Eyring–Powell flow in a stretching channel with chemical reactions. *Physica A: Statistical Mechanics and its Applications*, *544*, p.124109.

[16] Aneja, M. and Sharma, S., 2019. Numerical study of bioconvection flow of nanofluids using non-Fourier's heat flux and non-Fick's mass flux theory. *International Journal of Modern Physics B*, *33*(31), p.1950376.

[17] Shaik, J., Polu, B.A.R., Mohamed Ahmed, M. and Ahmed Mohamed, R., 2022. Characteristics of moving hot block and non-Fourier heat flux model on sinusoidal wavy cavity filled with hybrid nanofluid. *The European Physical Journal Plus*, *137*(1), p.131.

[18] Ibrahim, W., 2018. Three dimensional rotating flow of Powell-Eyring nanofluid with non-Fourier's heat flux and non-Fick's mass flux theory. *Results in physics*, *8*, pp.569-577.

[19] Mabood, F., Imtiaz, M., Rafiq, M., El-Zahar, E.R., Sidi, M.O. and Khan, M.I., 2022. Bidirectional rotating flow of nanofluid over a variable thickened stretching sheet with non-Fourier's heat flux and non-Fick's mass flux theory. *PLoS one*, *17*(4), p.e0265443.

[20] Ibrahim, W., Gamachu, D. and Feyisa, M., 2022. Computational study of micro-polar nanofluid past a spinning disk with non-Fourier's heat and non-Fick's mass flux models. *Waves in Random and Complex Media*, pp.1-22.

[21] Nasir, M., Waqas, M., Kausar, M.S., Bég, O.A. and Zamri, N., 2022. Cattaneo-Christov dual diffusive non-Newtonian nanoliquid flow featuring nonlinear convection. *Chinese Journal of Physics*.

[22] Malik, R., Khan, M., Shafiq, A., Mushtaq, M. and Hussain, M., 2017. An analysis of Cattaneo-Christov double-diffusion model for Sisko fluid flow with velocity slip. *Results in physics*, *7*, pp.1232-1237.

[23] Loganathan, K., Alessa, N., Namgyel, N. and Karthik, T.S., 2021. MHD flow of thermally radiative Maxwell fluid past a heated stretching sheet with Cattaneo–Christov dual diffusion. *Journal of Mathematics*, *2021*, pp.1-10.

[24] Dadheech, P.K., Agrawal, P., Sharma, A., Dadheech, A., Al-Mdallal, Q. and Purohit, S.D., 2021. Entropy analysis for radiative inclined MHD slip flow with heat source in porous medium for two different fluids. *Case Studies in Thermal Engineering*, *28*, p.101491.

[25] Bejawada, S.G., Reddy, Y.D., Jamshed, W., Nisar, K.S., Alharbi, A.N. and Chouikh, R., 2022. Radiation effect on MHD Casson fluid flow over an inclined non-linear surface with chemical reaction in a Forchheimer porous medium. *Alexandria Engineering Journal*, *61*(10), pp.8207-8220.

[26] Prasanna Jeyanthi, M. and Ganesh, S., 2022. Numerical solution of steady MHD duct flow in a square annulus duct under strong transverse magnetic field. *International Journal of Ambient Energy*, *43*(1), pp.2816-2823.

[27] Shohet, J.L., 1962. Velocity and temperature profiles for laminar magnetohydrodynamic flow in the entrance region of an annular channel. *The Physics of Fluids*, *5*(8), pp.879-884.

[28] Delhi Babu, R., Ganesh, S. and Kirubhashankar, C.K., 2022. An exact solution of Unsteady Magnetohydrodynamic flow of Dusty fluid between parallel porous plates with an angular velocity. *International Journal of Ambient Energy*, *43*(1), pp.1942-1948.

[29] Moresco, P. and Alboussiere, T., 2004. Experimental study of the instability of the Hartmann layer. *Journal of Fluid Mechanics*, *504*, pp.167-181.

[30] Vimala, P. and Manimegalai, K., 2021. Mixed Convection MHD Flow of a Nanofluid in a Rotating System with Heat Generation/Absorption. In *Fluid Mechanics and Fluid Power: Proceedings of FMFP 2019* (pp. 315-323). Springer Singapore.

[31] Li, W. and Fan, S., 2018. Nanophotonic control of thermal radiation for energy applications. *Optics express*, *26*(12), pp.15995-16021.

[32] Safaei, M.R., Karimipour, A., Abdollahi, A. and Nguyen, T.K., 2018. The investigation of thermal radiation and free convection heat transfer mechanisms of nanofluid inside a shallow cavity by lattice Boltzmann method. *Physica A: Statistical Mechanics and Its Applications*, *509*, pp.515-535.

[33] Al-Khaled, K., Khan, S.U. and Khan, I., 2020. Chemically reactive bioconvection flow of tangent hyperbolic nanoliquid with gyrotactic microorganisms and nonlinear thermal radiation. *Heliyon*, *6*(1).

[34] Gnaneswara Reddy, M., Sudharani, M.V.V.N.L., Ganesh Kumar, K., Chamkha, A.J. and Lorenzini, G., 2020. Physical aspects of Darcy–Forchheimer flow and dissipative heat transfer of Reiner–Philippoff fluid. *Journal of Thermal Analysis and Calorimetry*, *141*, pp.829-838.

[35] Hayat, T., Muhammad, T., Alsaedi, A. and Alhuthali, M.S., 2015. Magnetohydrodynamic three-dimensional flow of viscoelastic nanofluid in the presence of nonlinear thermal radiation. *Journal of Magnetism and Magnetic Materials*, *385*, pp.222-229.

[36] Wakif, A., Chamkha, A., Thumma, T., Animasaun, I.L. and Sehaqui, R., 2021. Thermal radiation and surface roughness effects on the thermo-magneto-hydrodynamic stability of alumina–copper oxide hybrid nanofluids utilizing the generalized Buongiorno's nanofluid model. *Journal of Thermal Analysis and Calorimetry*, *143*, pp.1201-1220.

[37] Saeed, A., Tassaddiq, A., Khan, A., Jawad, M., Deebani, W., Shah, Z. and Islam, S., 2020. Darcy-Forchheimer MHD hybrid nanofluid flow and heat transfer analysis over a porous stretching cylinder. *Coatings*, *10*(4), p.391.

[38] Khan, M.I., Al-Khaled, K., Khan, S.U., Muhammad, T., Waqas, H., El-Refaey, A.M. and Khan, M.I., 2021. Dynamic consequences of nonlinear radiative heat flux and heat generation/absorption effects in cross-diffusion flow of generalized micropolar nanofluid. *Case Studies in Thermal Engineering*, *28*, p.101451.

[39] Khan, S.U., Alam, M.M., Ghachem, K., Kolsi, L., Asiri, S.A., Gorji, M.R. and Chammam, W., 2022. Thermally radiative flow of Williamson nanofluid containing microorganisms with applications of heat source and activation energy. *International Journal of Modern Physics C*, *33*(09), p.2250125.

[40] Pop, I. and Sheremet, M., 2017. Free convection in a square cavity filled with a Casson fluid under the effects of thermal radiation and viscous dissipation. *International Journal of Numerical Methods for Heat & Fluid Flow*, *27*(10), pp.2318-2332.

[41] Bhatti, M.M., Abbas, T. and Rashidi, M.M., 2016. Effects of thermal radiation and electromagnetohydrodynamics on viscous nanofluid through a Riga plate. *Multidiscipline Modeling in Materials and Structures*, *12*(4), pp.605-618.

[42] Javed, T., Ali, N., Abbas, Z., & Sajid, M. (2013). Flow of an Eyring-Powell non-Newtonian fluid over a stretching sheet. *Chemical Engineering Communications*, *200*(3), 327-336.

[43] Liao, S. (2010). An optimal homotopy-analysis approach for strongly nonlinear differential equations. *Communications in Nonlinear Science and Numerical Simulation*, *15*(8), 2003-2016.

[44] Hayat, T., Muhammad, T., Alsaedi, A., & Ahmad, B. (2016). Three-dimensional flow of nanofluid with Cattaneo–Christov double diffusion. *Results in physics*, *6*, 897-903.

[45] Hayat, T., Aziz, A., Muhammad, T., & Alsaedi, A. (2017). On model for flow of Burgers nanofluid with Cattaneo–Christov double diffusion. *Chinese Journal of Physics*, *55*(3), 916-929.